

# Phased Array Characterization of Slat Noise Radiation from a High-Lift Common Research Model

William M. Humphreys, Jr.<sup>\*</sup>, David P. Lockard<sup>‡</sup>, Christopher J. Bahr<sup>§</sup>  
*NASA Langley Research Center  
Hampton, Virginia 23681-2199*

A test campaign was conducted in the open-jet test section of the NASA Langley 14- by 22-Foot Subsonic Tunnel on a 10%-scale, semispan version of a High-Lift Common Research Model (CRM-HL) incorporating a leading-edge slat, trailing-edge flap and removable high-fidelity main landing gear. Far field acoustic measurements were obtained on baseline and acoustically treated model configurations using a traversing 97-microphone phased array that viewed the pressure side of the airframe. A modified version of the DAMAS deconvolution method incorporating corrections for shear layer acoustic wave decorrelation was employed to determine the locations and strengths of relevant noise sources along the span of the slat and in the vicinity of the flap edges and landing gear. The main goal of the test campaign was to use the array data to evaluate the effectiveness of various slat noise reduction concepts. It was found that slat-gap fillers produced significant broadband noise reduction for all Mach numbers and airfoil angles of attack that were investigated. Mach number scaling revealed an approximate velocity to the sixth power relationship for the slat noise at higher frequencies. Directivity measurements obtained from integration of DAMAS pressure-squared values over defined geometric zones around the model showed that baseline slat noise radiation approximated a dipole as a function of polar emission angle, becoming approximately omnidirectional with the introduction of the slat-gap filler. The test campaign clearly demonstrated the noise reduction benefits that can be obtained by applying appropriate treatments to leading edge slats on commercial transport-class aircraft.

## Nomenclature

$\alpha$	= angle of attack, degrees
$f$	= frequency, Hertz
$f_m$	= model scale frequency, Hertz
$\Phi$	= array station, degrees
$\theta_e$	= polar emission angle, degrees
$CSM$	= Cross Spectral Matrix
$CRM-HL$	= High-Lift Common Research Model
$DAMAS$	= Deconvolution Approach for the Mapping of Acoustic Sources
$FSS$	= Full-Span Slat
$M$	= Mach number
$MCF$	= Mutual Coherence Function
$MLG$	= Main Landing Gear
$PSS$	= Part-Span Slat
$SCF$	= Slat-Cove Filler
$SGF$	= Slat-Gap Filler
$SPL$	= Sound Pressure Level, dB

---

<sup>\*</sup>Aerospace Engineer, Research Directorate, Associate Fellow AIAA

<sup>‡</sup>Aerospace Engineer, Computational AeroSciences Branch, Associate Fellow AIAA

<sup>§</sup>Aerospace Engineer, Aeroacoustics Branch, Associate Fellow AIAA

## I. Introduction

The NASA Aeronautics Research Mission Directorate's Advanced Air Transport Technology (AATT) Project includes as one of its baseline goals the understanding and mitigation of radiated noise from high-lift systems on commercial-class transonic aircraft. Slat noise has been identified as a prominent source of airframe noise during aircraft approach and landing, competing with noise generated by trailing edge flaps and the aircraft undercarriage. The reduction of slat noise requires a synergistic experimental assessment of the baseline noise generated by unmodified slat structures, coupled with high-fidelity numerical simulations of the flow-induced noise mechanisms on these structures. An understanding of the noise generation mechanisms can then drive the development and deployment of practical and effective noise mitigation concepts. Over the past two decades a number of experimental and computational studies have been performed to understand and model the noise generated by leading edge slats (for a generic geometry see Figure 1) [1-7].

Previous measurements by Moriarty, et al. [8] have shown the flow through the slat gap to be at a much higher speed than the freestream flow. Moriarty also found the highest turbulent kinetic energy levels in the slat gap region, where reattachment of the separated shear layer occurs. These findings suggest the slat gap flow to be a dominant source of radiated noise. This implies that modification of the flow through the gap could be an effective way of mitigating slat noise. This was the goal of the current study, based on testing of an instrumented, 10%-scale, semispan High-Lift Common Research Model (CRM-HL) installed in the NASA Langley 14- by 22-Foot Subsonic Tunnel (14x22) in the Fall of 2020.

An objective of the wind tunnel campaign was to characterize the nature of baseline and treated slat noise radiation via (1) identification of noise source regions on the model, (2) quantification of the noise source strengths, (3) measurement of radiated noise directivity, and (4) comparison with computational simulations of the noise. The characterization was conducted using a traversing microphone phased array mounted along the sidewall of the tunnel test section viewing the pressure side of the model. Figure 2 depicts the traversing array installed in the 14x22 tunnel. A modified version of the DAMAS beamforming and point spread function (PSF) deconvolution code incorporating corrections for shear layer decorrelation [22] was used to obtain noise contour presentations and directivity for acoustic sources present on the model. This paper presents a detailed characterization of the noise radiated by the leading-edge slat, both baseline and with noise reduction treatments added. Presentations include integrated spectra of noise source regions along with Mach number, angle of attack, and directivity effects.

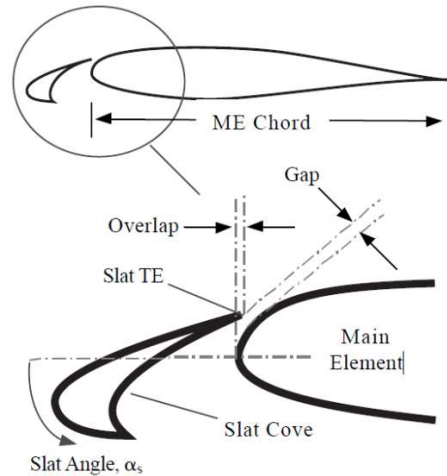


**Figure 1. Generic leading edge slat geometry (from Ref. 7).**

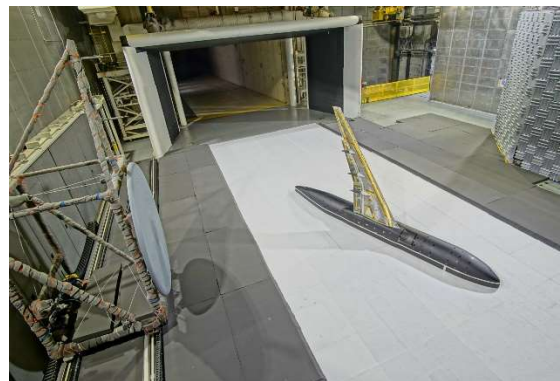


**Figure 2. Phased array viewing pressure side of the CRM-HL, looking downstream in the 14x22 tunnel. (Source: NASA)**

## II. Test Description

**Tunnel:** The 14- by 22-Foot Subsonic Tunnel (Figure 3) is an atmospheric, closed-return tunnel that has the capability to test a variety of fixed and rotary wing aircraft and test articles, both powered and unpowered. The tunnel has a contraction area ratio of 9:1. Using a 12,000 horsepower drive system, the tunnel can generate airflows up to Mach 0.3, corresponding to a maximum unit Reynolds number of  $7.2 \times 10^6$  per meter ( $2.2 \times 10^6$  per foot). The test section has dimensions of 4.42-meters (14.5-feet) high by 6.63-meters (21.75-feet) wide by 15.25-meters (50-feet) long and was configured for partial open-jet (floor in place) operation for the present study. For acoustic testing, the floor of the test section was lowered approximately 0.6 meters (2 feet) to permit the installation of rigid steel frame baskets containing sound absorbing acoustic foam wedges topped with foam sheets and perforated metal panels. The perforated panels were covered by an adhesive felt layer to reduce floor scrubbing noise (see Fig. 2). Additionally, foam sheets were applied to the floors outside of the test section. A combination of acoustic foam wedges and perforated panels were attached to the raised ceiling and outer sidewalls of the test section. When combined with the floor baskets, these treatments created an effective semianechoic environment in the open-jet test section that minimized unwanted acoustic reflections. A detailed series of empty tunnel noise measurements were conducted at the conclusion of the CRM-HL test campaign to characterize the background noise levels in the facility as a function of Mach number and array location. For the CRM-HL noise spectra presented here, the tunnel noise floor for the majority of the Mach numbers tested was deemed acceptable. Additional details regarding the background noise characterizations and the noise reduction treatments applied to the tunnel are described by Hutcheson, et al. [9].

**Model:** The model tested for this study was a 10%-scale version of the CRM-HL developed by Lacy and Sclafani [10] with a 2.938-meter (9.7-foot) semispan and a 0.7-meter (2.3-foot) mean aerodynamic chord. The model represented an open geometry and consisted of a supercritical transonic wing with a fuselage representative of a widebody commercial transport vehicle. The full model was comprised of a fuselage, wing, inboard and outboard trailing edge flaps (meeting at the center), inboard and outboard leading-edge slats, a pylon and flow-through nacelle, and a high-fidelity main landing gear. Two slat configurations were available for testing: (1) a full-span slat (FSS, Figure 4) where the pylon and nacelle were removed and replaced with a bridge section, and (2) a part-span slat (PSS, Figure 5) where the pylon and nacelle were in place. For the approach and landing configuration tested here, the flap



**Figure 3. Aerial view of the Langley 14- by 22-Foot Tunnel (Source: NASA).**



**Figure 4. CRM-HL FSS Configuration (Source: NASA).**



**Figure 5. CRM-HL PSS Configuration (Source: NASA).**

deflection was set to 37 degrees and the slat deflections set to 30 degrees. The model geometry included fifteen slat brackets, three flap brackets, and flap track fairings. The slat brackets employed in this investigation were more realistic (in terms of curvature and the location that they emanate from the main-element) than those previously tested. [16] The model was heavily instrumented with static pressure taps distributed on the main element, flap and slat, and a number of unsteady pressure transducers situated along the span of the baseline slat and main-element leading edge. More detailed descriptions of the model construction and instrumentation can be found in Refs [11, 12].

Two slat noise reduction concepts were tested for this study: (1) a slat cove filler (SCF), and (2) a slat gap filler (SGF). [13 – 16] The current study focused on deployable SCF and SGF hardware fabricated out of nickel-titanium shape-memory alloy (SMA) to allow the slat to be retracted, although the model was not actually articulated for this study. Only the SGF noise data are presented here. A complete ensemble of model configurations was tested as part of the wind tunnel campaign. A subset of these is presented in this paper and summarized in Table 1.

**Table 1. Model Configurations Presented in Paper.**

Configuration #	Full-span Slat (FSS)	Part-span Slat w/Nacelle (PSS)	Slat Gap Filler (SGF)	Main Landing Gear (MLG)
1	X			
2		X		
3	X		X	
4		X	X	
5	X		X	X
6		X	X	X

**Phased Array:** The phased array incorporated 97 Bruel and Kjaer (B&K) Model 4938 0.635-cm (1/4-inch) pressure field microphones attached to Model 2670 0.635-cm (1/4-inch) preamplifiers powered by B&K NEXUS® 2690 four-channel conditioning supplies.† Microphone signals were transmitted to the data acquisition system in the tunnel control room via LEMO microphone cables. The microphones were flush mounted (gap free) in a flat fiberglass honeycomb plate with total diameter of 2.45 meters (8.05 feet). The array was designed for an operational frequency range of approximately 1.5 kHz to 80 kHz. This was achieved by using an irregular circular pattern of microphones comprised of 16 array arms with 6 microphones in each arm (see Figure 6). One microphone was positioned in the center of the array. The maximum array aperture size (outermost microphone to outermost microphone) was 2 meters (6.55 feet), yielding a solid collecting angle of 21.1 degrees at a working distance of 5.17 meters (16.96 feet) from the array face to the center of the test section [17]. The array was attached to a rigid aluminum mounting frame that was in turn mounted to two parallel 13.4-meter (44-foot) linear traversing rails on the “south” side of the test section (see Fig. 2). The linear rails permitted the array face to traverse the majority of the length of the test section.

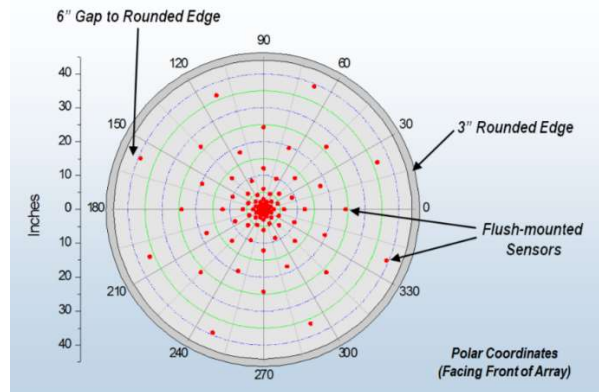


**Figure 6. 14- by 22-Foot Tunnel Traversing Phased Array Geometry.**

†Specific vendor and manufacturer names are explicitly mentioned only to accurately describe the test hardware. The use of vendor and manufacturer names does not imply an endorsement by the U.S. Government nor does it imply that the specified equipment is the best available.

**Data Acquisition:** A highly distributed data acquisition system using commercially available hardware was assembled for this study. The data system had a total capacity of 128 channels and provided signal conditioning and digitization for both the phased array microphones and auxiliary channels (unsteady pressure transducers, accelerometers, generated waveforms, and synchronization signals). Signal conditioning was provided by a Precision Filter 68000 system that provided programmable amplification and bandpass filtering. A custom digitization system based on General Standards 24-bit, 64-channel simultaneous sampling PCI cards was constructed and programmed by AVEC, Inc. for the test campaign. A National Instruments LabVIEW®-based program was developed and used for command and control of all of the hardware components of the data system as well as the linear traversing rails supporting the phased array. The nominal acquisition window length was 35 seconds with a simultaneous sampling rate of 196.608 kHz for all channels. The microphone signals were bandpass filtered from 1 - 60 kHz. Acquired microphone and auxiliary channel time history data were stored as a series of ensemble raw binary data files coupled with metadata companion files. These were subsequently converted into Hierarchical Data Format Version 5 (HDF5) files for long-term archiving [18].

**Data Reduction and Analysis:** The reduction of data obtained from the array microphones and auxiliary transducers consisted of several steps. Only brief descriptions of the data reduction steps are presented here. More detailed information can be obtained via the references below.

1. For each test point, a Cross Spectral Matrix (CSM) was generated in engineering units. A subspace background subtraction technique implemented by Bahr, et al. [19] and based on eigenvalue decomposition of background noise CSMs was used to remove tunnel circuit noise from the array spectral measurements. An optimized CSM diagonal modification was also employed [20] to remove microphone self-noise from the measurements, though this was found to have minimal influence on the results when used in conjunction with background subtraction.
2. Detailed analysis of the array data was performed using conventional frequency-domain delay and sum beamforming. This was coupled with the DAMAS point spread function deconvolution algorithm [21] for generation of final noise source map presentations. The DAMAS algorithm was modified by Bahr [22] to correct for randomization of the propagation path through the turbulence of the tunnel open-jet shear layer. This randomization effect results in coherence loss between microphone pairs, reducing the spatial resolution of the array. The correction incorporates a Mutual Coherence Function (MCF) into the DAMAS propagation model. The MCF is measured using pseudo point sources (speakers) embedded at key locations on the pressure side of the CRM-HL wing, with the point source data acquired at similar tunnel conditions for model data runs. A turbulence model is applied to correct for measurement grid locations away from the point sources. The beamforming and iterative relaxation solver portions of DAMAS remain unchanged. An error function-based array shading algorithm was employed to control the beamwidth of the array across the measured frequency range [23]. The modified DAMAS algorithm is referred to as MCF-DAMAS here.
3. Figure 7 shows the spatial regions that were defined around the model in order to compute 1/12<sup>th</sup>-octave Sound Pressure Level (SPL) integrated spectra for this study. Zone 1 (shown in red in Fig. 7) represents integration of the entire wing region and is used diagnostically to compare test points where the effects of trailing edge flap, nacelle, and/or landing gear noise are desired. Zone 2 (shown in blue in Fig. 7) represents

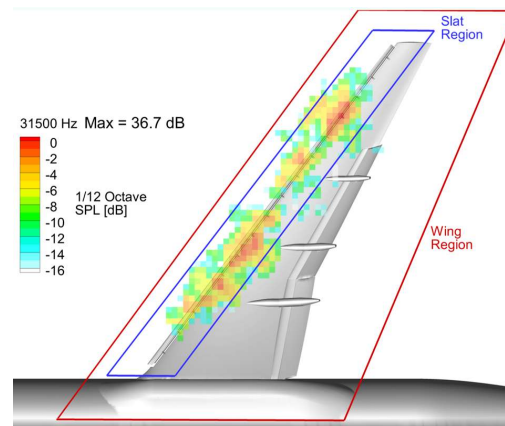


**Figure 7. Source Integration Regions:  
Zone 1 – Red, Zone 2 – Blue.**

integration of the leading edge slat region in isolation and is used diagnostically to compare baseline and treated slat noise. For each of these two zones, the spectral levels were obtained on a narrowband basis ( $\Delta f = 96$  Hz) by simple summing of the mean squared pressures generated by MCF-DAMAS deconvolution over the region(s) of interest. These were then converted to 1/12<sup>th</sup>-octave bands. All spectral data presented are based on model scale frequencies. Pressure doubling due to flush mounting of the array microphones has been removed and ray path distance corrections for the various array observer locations are included. It is noted that the Zone 1 and Zone 2 integrated spectra for the CRM-HL are similar as almost all of the strong sources are in the slat region.

### III. Results and Discussion

Unless otherwise stated, results are shown for a model angle of attack of 8.5 degrees. The microphone array was positioned at a number of streamwise observer locations with respect to the center of rotation of the model fuselage (the defined reference location on the model). These array stations spanned 70 to 120 degrees in 10 degree increments with an additional station at 56 degrees included in the test matrix (this was the farthest upstream that the array could be traversed in the tunnel test section). Equivalent polar emission angles were determined from the open-jet shear layer refraction using Amiet's method (see Appendix I). [24] All spectra presented in this section were verified accurate via examination of at least two repeat test points for quality in each case. For brevity, these repeat points are not shown here.

Baseline Model Geometry – FSS (Configuration 1): Figure 8 depicts MCF-DAMAS deconvolved source distribution maps showing predominant baseline FSS noise generation regions for a number of 1/12-octave center frequencies spanning 2 – 35 kHz. In each contour presentation, the dB levels have been normalized to the local peak level shown in the map with a total range of 16 dB presented. At lower frequencies, noise radiation from the outer outboard slat region and wing tip dominate, along with contributions from the flap brackets and fairings. Interestingly, at 8 kHz the noise radiation is dominated by a tone-related hot spot occurring in the vicinity of the FSS bridge section. It has been noted [12] that the location of this tone varied with every model configuration and tunnel condition, implying that the conditions needed to produce this resonance are highly dependent on the model geometry and flow. At higher frequencies, the noise radiation is more uniform across the span of the slat region with some individual concentrations of noise observed from a few of the slat brackets. Flap noise is not a significant contributor to the overall noise above 6 kHz.

Figure 9 shows the effects of angle of attack on the integrated noise spectra for Zone 2 on the model. As expected, there is a clear angle of attack dependency on the overall spectral levels, with a roughly 5 dB increase observed as  $\alpha$  increases from 4 to 13 degrees. It is noted that the spectral shapes observed at all  $\alpha$  values are relatively similar with the exception of the observed tones in the 7 - 12 kHz range. There is an observed collapse of the spectra below 1.5 kHz that may be attributable to prevalent non-slat sources below 2 kHz as well as background noise source effects.

The effect of Mach number variation on the measured noise spectra integrated over Zone 2 is shown in Figure 10. While the spectral features are similar at all flow speeds, there is an expected rise in overall SPL as a function of Mach number. Figure 11 shows the scaling of the Figure 10 spectra assuming a sixth power dependency on flow speed. No Strouhal frequency scaling has been performed. Above 15 kHz, the collapse of the spectra is excellent; however, below approximately 4 - 5 kHz, the collapse appears to illustrate a fifth power dependency on flow speed versus a sixth power. The scaling law in the vicinity of the tones is uncertain. It is noted that the tones are resonance phenomena dependent on both geometric and flow characteristics, so frequency and amplitude scaling with speed are unlikely to follow any simple scaling [25, 26].

The effect of observer angle on the integrated noise spectra can be seen in Figure 12. Both the physical array observation stations and the equivalent polar emission angles are listed in the figure for

reference. At the upstream viewer locations, there are clear decreases in the overall noise level with less variation observed at downstream locations. The structure of the spectra is invariant with observer angle for frequencies away from the 7.5-kHz tonal peaks. Previous investigations of leading-edge slat noise by Mendoza, et al. [7] showed omnidirectional source characteristics at lower frequencies; however, this is not observed in the present data.

It has been postulated that the baseline slat noise acts as an approximate dipole source. This was investigated for this study by applying a simple dipole scaling function to the directivity spectra, similar to that shown by Mendoza [7]. The spectral normalization takes the form of

$$SPL_{scaled} = SPL - [10 * \log \left( \frac{\sin^2 \theta_e}{(1+M \cos \theta_e)^4} \right)]. \quad (1)$$

Figure 13 depicts the results of application of Equation (1) to the baseline FSS directivity. The amplitude scaling utilizes the polar emission angles obtained from the tunnel open-jet shear layer refraction, and includes dB corrections to account for shear layer ray path differences at the various observer locations. The scaling does an excellent job of collapsing the spectra across the entire frequency range, especially at frequencies below 10 kHz, and confirms the dipole nature of the radiated slat noise.

Baseline Model Geometry – PSS (Configuration 2): Figure 14 depicts MCF-DAMAS deconvolved source distribution maps showing predominant baseline PSS noise generation regions for a number of 1/12-octave center frequencies spanning 2 – 35 kHz. As in Figure 8, the dB levels have been normalized to the local peak level shown in each map with a 16 dB range shown. At frequencies below 20 kHz, the noise generated in the vicinity of the outboard edge of the inboard slat dominates, likely due to slat bracket and gap flow interactions near the pylon. The noise radiation from this area peaks around 8 kHz and has been observed across a range of Mach numbers. Above 20 kHz, the noise is more distributed along the span of the outboard slat, although at 25 kHz a predominant noise source appears at the inboard edge of the outboard slat near the pylon. Only minimal flap noise is observed at all frequencies. Some noise is observed in the floor region in front of the fuselage above 20 kHz. It is speculated that the source of this noise is a horseshoe vortex interacting with the fuselage and floor when the model is generating significant lift [9]. Subsequent treatment via the application of felt to the offset on the fuselage eliminated this noise source.

The effect of Mach number variation on the baseline PSS measured noise spectra, integrated over Zone 2, is shown in Figure 15. The spectral features below approximately 7 kHz are somewhat similar at all flow speeds. As noted previously, the observed broad tonal features that represent multiple narrow band peaks are produced in the vicinity of the inboard edge of the outboard slat and appear to approximately adhere to Strouhal scaling from their noted locations in the figure. The observed rise in spectral levels above 20 kHz for the lower Mach numbers matches the observed increase in distributed noise along the span of the outboard slat in Figure 14. Figure 16 shows the scaling of the Figure 15 spectra assuming a sixth power dependency on flow speed. Above 15 kHz, the collapse of the spectra is excellent; however, below approximately 4 - 5 kHz, the collapse again appears to depend more on a fifth power of flow speed versus a sixth power, although the effect is not as pronounced as for the baseline FSS. The velocity scaling law in the vicinity of the tones is again uncertain.

The baseline PSS directivity is represented in Figure 17 for observer locations spanning 56 to 120 degrees. In general, the addition of the pylon does not appear to significantly affect the directivity for most frequencies, and the spectral variation shown in the figure is remarkably similar to that shown in Figure 12. Figure 18 shows the directivity scaled using a dipole assumption and the spectral normalization of Equation (1). Below 20 kHz, the collapse of the spectra is excellent confirming dipole behavior; however, there is some residual scatter shown above 20 kHz for currently unknown reasons. It is speculated that tonal noise radiation due to flow interactions around the pylon may contribute to this variation in dB levels since such radiation could be directed more to downstream observers.

Slat Gap Filler – FSS (Configuration 3): It was anticipated that the introduction of a gap filler would significantly reduce the noise generated by the leading edge slat due to disruption of the flow through the gap. This is confirmed in Figure 19 where MCF-DAMAS deconvolved source distribution maps derived from analyses of the full-span slat with a slat-gap filler were conducted. The model configuration shown in Figure 14 includes full blockage slat tips in addition to the filler [15]. The slat noise has effectively been eliminated for the majority of 1/12-octave frequencies via the introduction of the gap filler, with the exception of some remaining slat noise at 6 kHz. There is also residual noise observed at the wingtip for a number of lower and mid frequencies. This noise could be a combination of wing tip vortex noise and outboard slat / slat tip noise. A small slat tonal spot appears at 4 kHz with a more prominent one appearing at 10 kHz. These were likely due to flow through a small gap between the tip treatment and the rest of the slat and were later eliminated via application of clay and tape in these regions. With the reduction of the slat noise, the flap noise now appears as a dominant (but still low-level) noise generation mechanism, with outer flap edge and bracket noise appearing for many of the frequencies shown in Figure 19.

Figure 20 presents a comparison of the integrated noise spectra for the baseline FSS versus the FSS with the added SGF. Dramatic reductions of up to 10 dB in the spectral levels are shown in the comparison for all observer angles, especially above 3 kHz. The broadband tonal structure occurring around 7.5 kHz for the baseline FSS has been completely eliminated, although a few new tones are appearing at approximately 11 and 22 kHz for the FSS/SGF configuration, perhaps emanating from a gap in the bridge piece end.

The effect of Mach number scaling on the measured FSS/SGF noise spectra integrated over Zone 2 is shown in Figure 21. As with Figure 16, a sixth power dependency on flow speed is assumed, resulting in an excellent collapse of the spectra. Curiously, the fifth power dependency observed for the baseline FSS at lower frequencies does not appear when the SGF is added, although there is a notable deficit in the spectral level at Mach 0.12 for frequencies less than 5 kHz. In addition, two significant tones are observed at approximately 7 and 16 kHz in the Mach 0.12 spectrum.

It was anticipated that the addition of the SGF would affect the directivity of the slat and this is confirmed in Figure 22. The dipole directivity observed for the baseline FSS in Figure 17 has been replaced with approximate omnidirectional noise across the entire frequency span for the FSS/SGF configuration, although there is still some variation as a function of observer angle. In general, lower spectral levels are shown at upstream locations with somewhat higher levels seen at downstream locations. The exception to this is for  $\phi = 56^\circ$ , where the spectral levels at this observer angle relative to the levels at  $\phi = 90^\circ$  are greater for frequencies above 10 kHz than for frequencies lower than this.

Slat Gap Filler – PSS (Configuration 4): MCF-DAMAS deconvolved source distribution maps for the PSS/SGF configuration are shown in Figure 23. This model configuration, as described in Section II, includes full blockage slat tips. The introduction of the gap filler has again eliminated the majority of slat noise for most of the displayed 1/12-octave frequencies for this configuration, with the exception of some residual noise observed along the outboard slat between 4 and 8 kHz. There is also noise observed at the wingtip between 4 and 20 kHz, as well as a small broadband spot appearing at the aft end of the wing root for frequencies spanning 4 - 25 kHz. Flap bucket noise is somewhat more prominent for this configuration versus the FSS/SGF with significant noise observed for the outboard flap bracket at 8 kHz and the mid flap bracket at 20 kHz.

A comparison of baseline PSS noise with noise generated when the SGF is added can be seen in Figure 24. Similar to the FSS/SGF combination, the addition of the SGF to the PSS reduces the radiated noise by 10 dB for the majority of frequencies above 3 kHz. The Mach number scaling shown in Figure 25 confirms that this model configuration exhibits a sixth power velocity scaling. There is an excellent collapse of the spectral levels below 5 kHz with a somewhat less successful collapse at higher frequencies. The directivity data shown in Figure 26 confirms that this model configuration displays an approximate omnidirectional pattern over the ensemble of observer angles. The variation in spectral levels below 10 kHz is virtually identical to that shown in Figure 22, although there is more variability in

levels seen above 10 kHz for this configuration. In general, it can be concluded that the switch from Configuration 3 (FSS/SGF) to Configuration 4 (PSS/SGF) does not affect the radiated noise characteristics significantly, and that the addition of the flow-through nacelle has minimal impact on the observed noise.

Landing Gear Effects (Configurations 5 and 6): A high-fidelity main landing gear (MLG) was developed for the CRM-HL model (Figure 27). The gear assembly included a four-wheel truck attached to a clevis that allowed the truck angle to be set to  $-13^\circ$ ,  $0^\circ$ , or  $+13^\circ$ . High-fidelity components were constructed of stainless steel (load bearing) and nylon (nonload bearing) and included a door and scaled hydraulic lines and actuators. A partial landing gear bay was constructed within the main element wing. Additional drawings and details of the landing gear assembly can be found in Reference 11. For the MLG acoustic measurements shown here, the truck angle was set at a constant toe up angle of  $+13^\circ$ .

Figure 28 depicts MCF-DAMAS output for the FSS/SGF (Configuration 5) with the MLG attached. For this configuration, the noise is integrated over Zone 1 on the model. Not surprisingly, the MLG radiated noise is dominant. At lower frequencies (e.g., 2 kHz in the figure), flap bracket noise can also still be seen. With the SGF installed virtually, no slat noise is observed, with the one exception of residual outboard slat noise appearing at the wingtip at 2 kHz. It is noted that the MLG noise is not centered on the gear truck but is offset to the inboard side where the retraction brackets reside, indicating increased noise radiation from the brackets.

Figure 29 clearly shows the increase in noise for the Configuration 5. For the baseline FSS configuration (the black line in Figure 29), the addition of the gear (the green line) adds approximately 2-3 dB to the spectral levels across the entire frequency range. The effect is more dramatic for the FSS/SGF configuration (the red line) where the deployment of the gear (the blue line) adds 5-6 dB to the levels. Fortunately, in comparing the spectral levels for the FSS/MLG configuration with and without the SGF (green and blue lines), it is seen that the addition of the SGF lowers the observed noise levels by about 3-4 dB across the entire frequency range. Thus, the SGF provides an acoustic reduction benefit regardless of gear deployment for these configurations.

Figure 30 shows the Mach number scaling for the FSS/SGF/MLG combination. Previous investigations of scaled landing gear noise indicated a sixth power velocity scaling behavior [27]. This is confirmed in Figure 30 where an excellent collapse of the data is seen. Both the slat and landing gear contribute to a similar velocity scaling. There are strong tonal peaks shown at 7 kHz and 18 kHz, perhaps due to radiation from the flap brackets. These were seen in MCF-DAMAS outputs at Mach 0.12 for this configuration (not presented here).

Similar MCF-DAMAS presentations to those shown in Figure 28 can be seen in Figure 31 for the PSS/SGF with the MLG deployed (Configuration 6). The noise radiation characteristics for the MLG are virtually identical as compared with Configuration 5, and the MLG dominates the noise observed for all frequencies in Figure 31. This is not surprising since little to no slat / landing gear interaction is expected. Note that there were also no flap angle changes made that could influence the MLG noise. Figure 32 shows the increase in noise for the PSS/SGF/MLG configuration over the no-gear baseline. For the baseline FSS configuration (the black line in Figure 29), the addition of the gear (the green line) adds approximately 2 dB to the spectral levels across the entire frequency range. Using the PSS/SGF configuration (the red line) as a baseline, the deployment of the gear (the blue line) adds 5-6 dB to the levels. The noise behavior observed between Configurations 5 and 6 is virtually identical. Finally, the Mach number scaling depicted in Figure 33 again shows an excellent collapse of the spectra using a sixth-power scaling function. The same slat tones are observed as in Figure 30.

## IV. Summary

A detailed experimental study of the noise generated by a 10%-scale, semispan version of a High-Lift Common Research Model (CRM-HL) incorporating a leading-edge slat, trailing-edge flap and removable high-fidelity main landing gear was conducted in the open-jet test section of the NASA Langley 14- by 22-Foot Subsonic Tunnel. Acoustic measurements were obtained on baseline and acoustically treated model configurations using a traversing 97-microphone phased array that viewed the pressure side of the airframe. A modified version of the DAMAS array deconvolution method (MCF-DAMAS) was employed to determine the locations and strengths of relevant noise sources in the vicinity of the slat, flaps, and landing gear. Some primary conclusions derived from the study are as follows:

- The inclusion of the slat gap filler with slat tip transitions significantly reduced the radiated noise along the entire span of the slat, with typically 10 dB of noise reduction observed for the FSS/SGF and PSS/SGF configurations versus the baseline. There was some residual noise observed, especially near the wingtip, but not at significant levels. It can thus be concluded that the SGF is a very effective noise reduction mechanism for the slat.
- The flap noise was not a significant contributor to the overall radiated sound field for the baseline model configuration due to the stronger slat noise. With the addition of the SGF, the flap noise became more prominent but was still not a strong contributor to the overall noise. For certain configurations (Configuration 4 for instance), flap bracket noise could be observed for a number of frequencies due to the reduction in slat noise.
- Directivity measurements using the array at various observer locations revealed an approximate dipole directivity for the baseline FSS and PSS configurations. The incorporation of the SGF transitioned the radiated noise into an approximate omnidirectional pattern, although some residual variation with observer angle was seen, particularly for the PSS configurations.
- The observed Mach number variation implied a sixth power dependency on flow speed, although this only applied to higher frequencies for the baseline FSS and PSS configurations, with a fifth power dependency observed at lower frequencies. The addition of the SGF resulted in a true sixth power dependency across the entire frequency range. This is a somewhat unexpected finding, and it's not entirely clear why the scaling changes with the addition of the SGF.
- As expected, the addition of the untreated main landing gear dramatically increases the overall spectral levels, with noise radiation concentrated in the vicinity of the inboard side of the gear near the retraction brackets. There appears to be no interaction between the slat and the landing gear in terms of overall noise levels. The SGF provides effective noise reduction regardless of gear deployment.

Although beyond the scope of the analyses described in this paper, future work could include an examination of slat-cove filler effects for comparison with the slat-gap filler. There were many additional model configurations tested beyond the ones described here that could provide a rich source of comparison data.

## Acknowledgments

This work was sponsored by the NASA Advanced Air Transport Technology (AATT) Project in the Aeronautics Research Mission Directorate. The authors gratefully acknowledge the support and dedication of the 14- by 22-Foot Subsonic Tunnel staff, personnel from the NASA Langley Aeroacoustics, Structural Acoustics, and Computational Aerosciences Branches, and the many others who supported the test campaign.

## References

- [1] Guo, Y.P., “A Model for Slat Noise Generation”, AIAA Paper 1997-1647, 3<sup>rd</sup> AIAA/CEAS Aeroacoustics Conference, Atlanta, GA, 1997.
- [2] Storms, B.L., Ross, J.C., Horne, W.C., Hayes, J.A., Dougherty, R.P., Underbrink, J.R., Scharpf, D.F., and Moriarty, P.J., “An Aeroacoustic Study of an Unswept Wing with a Three-Dimensional High Lift System”, NASA Technical Memorandum 1998-112222, 1998.
- [3] Storms, B.L., Hayes, J.A., Moriarty, P.J., and Ross, C.J., “Aeroacoustic Measurements of Slat Noise on a Three-Dimensional High-Lift System”, AIAA Paper 1999-1957, 5<sup>th</sup> AIAA/CEAS Aeroacoustics Conference, Bellevue, WA, 1999.
- [4] Singer, B.A., Lockard, D.P., Brentner, K.S., Khorrami, M.R., Berkman, M.E., and Choudhari, M., “Computational Aeroacoustic Analysis of Slat Trailing Edge Flow”, AIAA Paper 1999-1802, 5<sup>th</sup> AIAA/CEAS Aeroacoustics Conference, Bellevue, WA, 1999.
- [5] Guo, Y.P., “A Discrete Vortex Model for Slat Noise Prediction”, AIAA Paper 2001-2157, 7<sup>th</sup> AIAA/CEAS Aeroacoustics Conference, Maastricht, Netherlands, 2001.
- [6] Dobrzynski, W., and Pott-Pollenske, M., “Slat Noise Source Studies for Farfield Noise Prediction”, AIAA Paper 2001-2158, 7<sup>th</sup> AIAA/CEAS Aeroacoustics Conference, Maastricht, Netherlands, 2001.
- [7] Mendoza, J.M., Brooks, T.F., and Humphreys, W.M., Jr., “An Aeroacoustic Study of a Leading Edge Slat Configuration”, *International Journal of Aeroacoustics*, Vol. 1(3), pp. 241-274, 2002.
- [8] Moriarty, P.J., and Heineck, J.T., “PIV Measurements Near a Leading Edge Slat”, Proceedings of the 3<sup>rd</sup> International Workshop on Particle Image Velocimetry (PIV), 1999.
- [9] Hutcheson, F.V., Lockard, D.P., and Stead, D.J., “On the Alleviation of Background Noise for the High-Lift Common Research Model Aeroacoustics Test”, 28<sup>th</sup> AIAA/CEAS Aeroacoustics Conference, Accepted, Southampton, UK, 2022.
- [10] Lacy, D.S., and Sclafani, A.J., “Development of the High-Lift Common Research Model (HL-CRM): A Representative High Lift Configuration for Transonic Transports”, AIAA Paper 2016-0308, AIAA SciTech 2016 Forum, San Diego, CA, 2016.
- [11] Fell, J.S., Webb, S.R., Laws, C.T., Snyder, M.L., and Rhew, R.D., “Development of the 10% NASA High-Lift Common Research Model (CRM-HL)”, AIAA Paper 2021-0385, AIAA SciTech 2021 Forum, 2021.
- [12] Lockard, D.P., Turner, T.L., Bahr, C.J., and Hutcheson, F.V., “Overview of Aeroacoustic Testing of the High-Lift Common Research Model”, AIAA Paper 2021-2113, AIAA Aviation 2021 Forum, 2021.
- [13] Streett, C.L., Casper, J.H., Lockard, D.P., Khorrami, M.R., Stoker, R.W., Elkoby, R., Wenneman, W.F., and Underbrink, J.R., “Aerodynamic Noise Reduction for High-Lift Devices on a Swept Wing Model”, AIAA Paper 2006-0212, 44<sup>th</sup> Aerospace Sciences Meeting, 2006.

- [14] Scholten, W.D., Hartl, D.J., Turner, T.L., and Kidd, R.T., “Development and Analysis-Driven Optimization of Superelastic Slat-Cove Fillers for Airframe Noise Reduction”, *AIAA Journal*, Volume 54(3), pp. 1078-1090, 2016.
- [15] Turner, T.L., and Long, D.L., “Development of a SMA-Based, Slat-Gap Filler for Airframe Noise Reduction”, AIAA Paper 2015-0730, AIAA SciTech 2015 Forum, Kissimmee, FL, 2015.
- [16] Turner, T.L., Mulvaney, J.W., Lockard, D.P., Allen, R.A., and Brynildsen, S.E., “Development of Slat Gap and Slat Cove Filler Treatments for Noise Reduction Assessment on the High-Lift Common Research Model in the NASA LaRC 14x22”, 28<sup>th</sup> AIAA/CEAS Aeroacoustics Conference, Accepted, Southampton, UK, 2022.
- [17] Humphreys, W. M., Brooks, T. F., Bahr, C. J., Spalt, T. B., Bartram, S. M., Culliton, W. G., and Becker, L. E., “Development of a Microphone Phased Array Capability for the Langley 14- by 22-foot Subsonic Tunnel”, *AIAA Paper 2014-2343*, 20<sup>th</sup> AIAA/CEAS Aeroacoustics Conference, Atlanta, GA, 2014.
- [18] Humphreys, W. M., Jr., “Microphone Phased Array NetCDF/HDF5 Archival Files: Application Program Interface Reference”, *NASA Technical Memorandum 2019-220402*, 2019.
- [19] Bahr, C. J. and Horne, W. C., “Subspace-based Background Subtraction Applied to Aeroacoustic Wind Tunnel Testing”, *International Journal of Aeroacoustics*, Vol. 16(4&5), pp. 299-325, 2017.
- [20] Hald, J., "Removal of Incoherent Noise from an Averaged Cross Spectral Matrix", *Journal of the Acoustical Society of America*, Vol. 142, pp. 846-854, 2017.
- [21] Brooks, T. F., and Humphreys, W. M., “A Deconvolution Approach for the Mapping of Acoustic Sources (DAMAS) Determined from Phased Microphone Arrays”, *Journal of Sound and Vibration*, Volume 294, pp. 856-879, 2006.
- [22] Bahr, C.J., “Accounting for the Influence of Decorrelation in Microphone Phased Array Deconvolution Methods”, 28<sup>th</sup> AIAA/CEAS Aeroacoustics Conference, Accepted, Southampton, UK, 2022.
- [23] Bahr, C.J., and Lockard, D.P., “Designing Shading Schemes for Microphone Phased Arrays”, BeBeC-2020-S1, 2020 Berlin Beamforming Conference, Berlin, Germany, 2020.
- [24] Amiet, R. K., “Refraction of Sound by a Shear Layer”, *Journal of Sound and Vibration*, Volume 58(4), pp. 467-482, 1978.
- [25] Jawahar, H.K., Meloni, R.C., and Azarpeyvand, M., “Intermittent and Stochastic Characteristics of Slat Tones”, *Physics of Fluids*, Vol. 33, 025120, 2021.
- [26] Ahlefeldt, T., “Microphone Array Measurement in European Transonic Wind Tunnel at Flight Reynolds Numbers”, *AIAA Journal*, Vol. 55(1), pp. 36-48, 2017.
- [27] Humphreys, W.M., Jr., and Brooks, T.F., “Noise Spectra and Directivity for a Scale-Model Landing Gear”, *International Journal of Aeroacoustics*, Vol. 8(5), pp. 409-443, 2009.

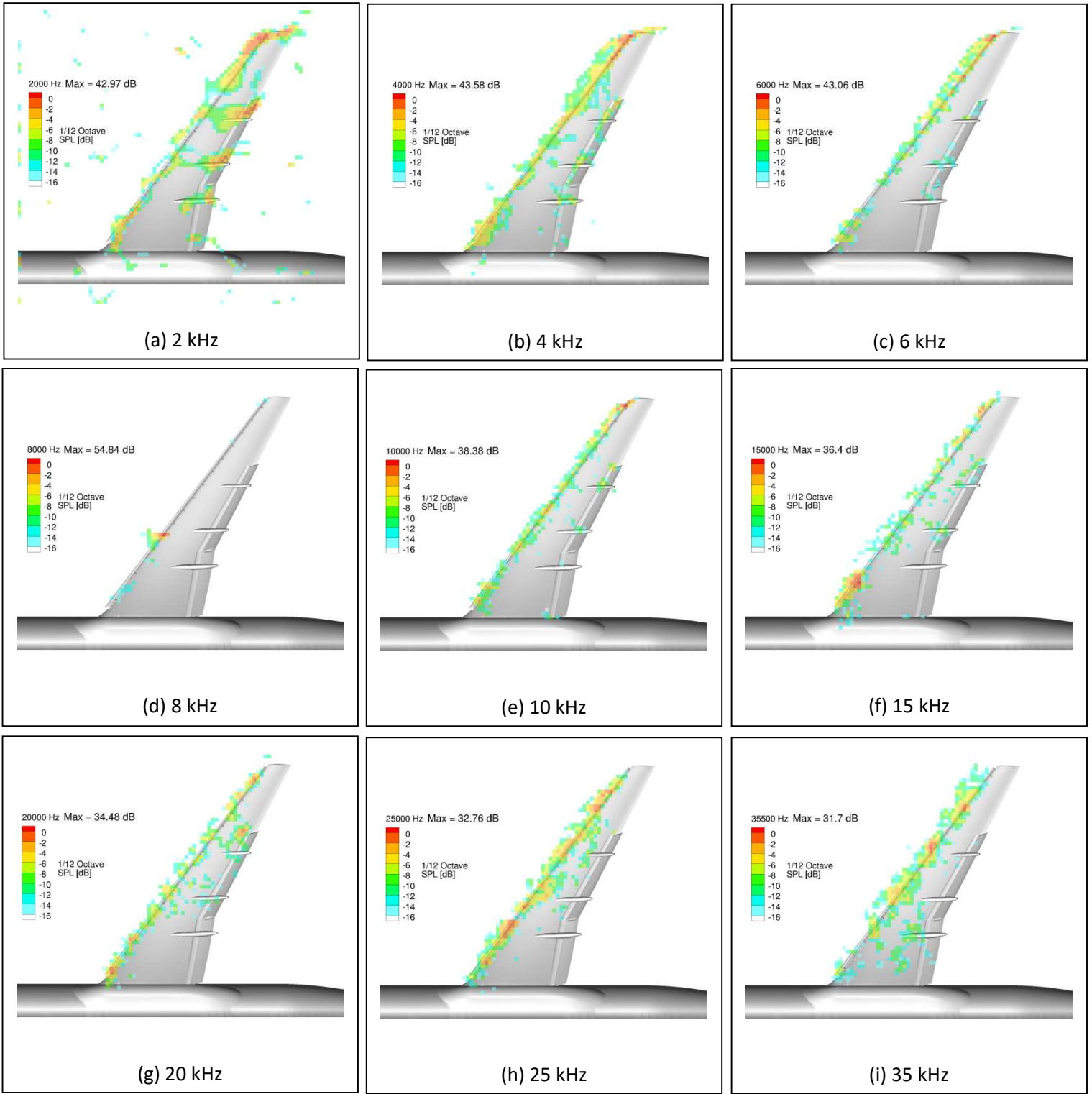


**Figure 8. 1/12-octave band MCF-DAMAS output.**  
**Baseline FSS (Configuration 1),  $\alpha = 8.5^\circ$ ,  $M = 0.16$ ,  $\phi = 90^\circ$ .**

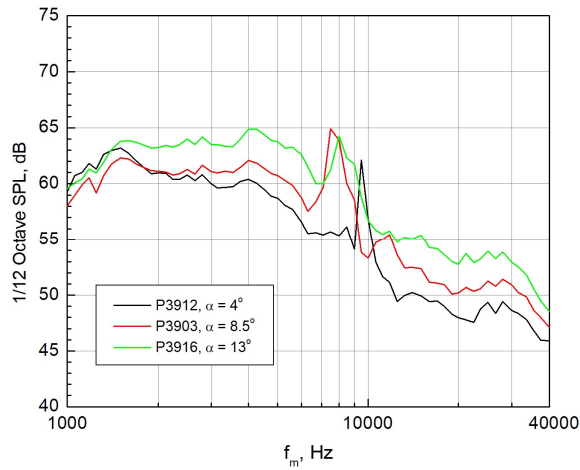


**Figure 9. Baseline FSS (Configuration 1)  
Angle of Attack Effects,  $M = 0.16$ ,  $\phi = 90^\circ$ .**

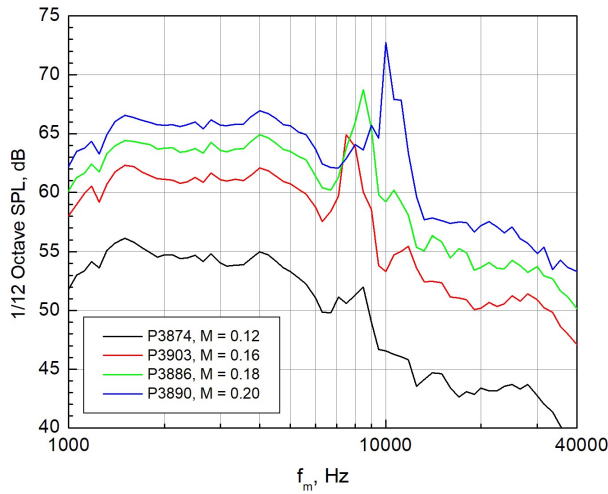


**Figure 10. Baseline FSS (Configuration 1)  
Mach Number Effects,  $\alpha = 8.5^\circ$ ,  $\phi = 90^\circ$ .**

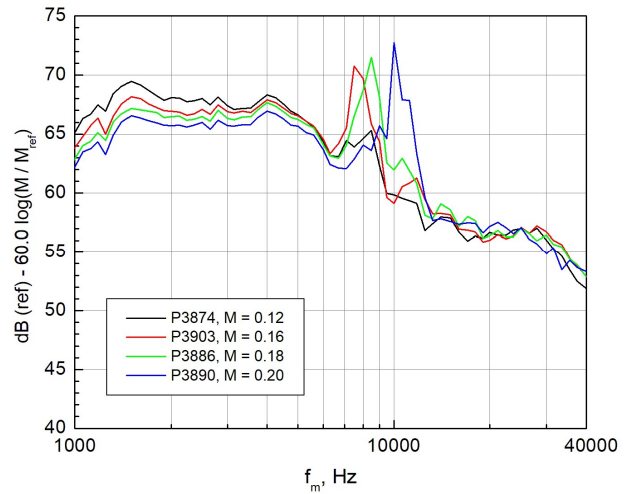


**Figure 11. Baseline FSS (Configuration 1)  
Mach Number Scaling,  $\alpha = 8.5^\circ$ ,  $\phi = 90^\circ$ .**

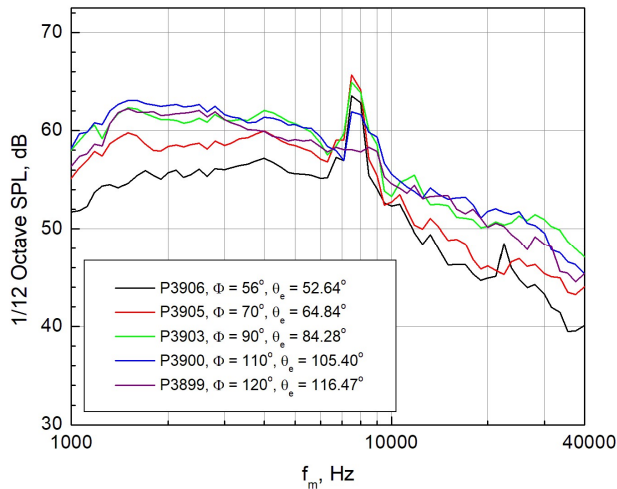


**Figure 12. Baseline FSS (Configuration 1)  
Directivity,  $\alpha = 8.5^\circ$ ,  $M = 0.16$ .**

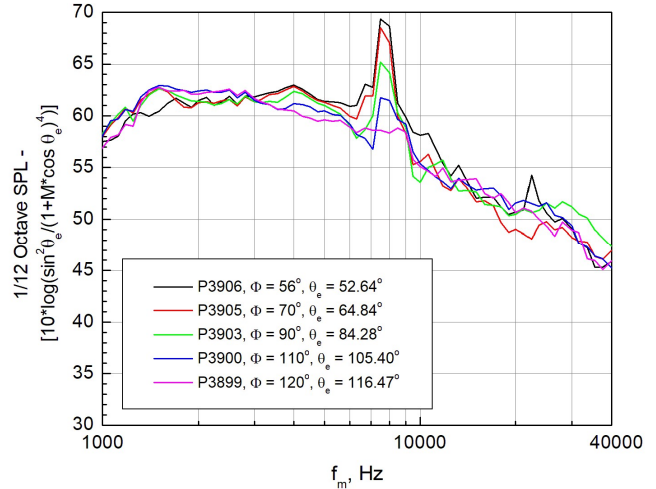


**Figure 13. Baseline FSS (Configuration 1)  
Scaled Directivity,  $\alpha = 8.5^\circ$ ,  $M = 0.16$ .**

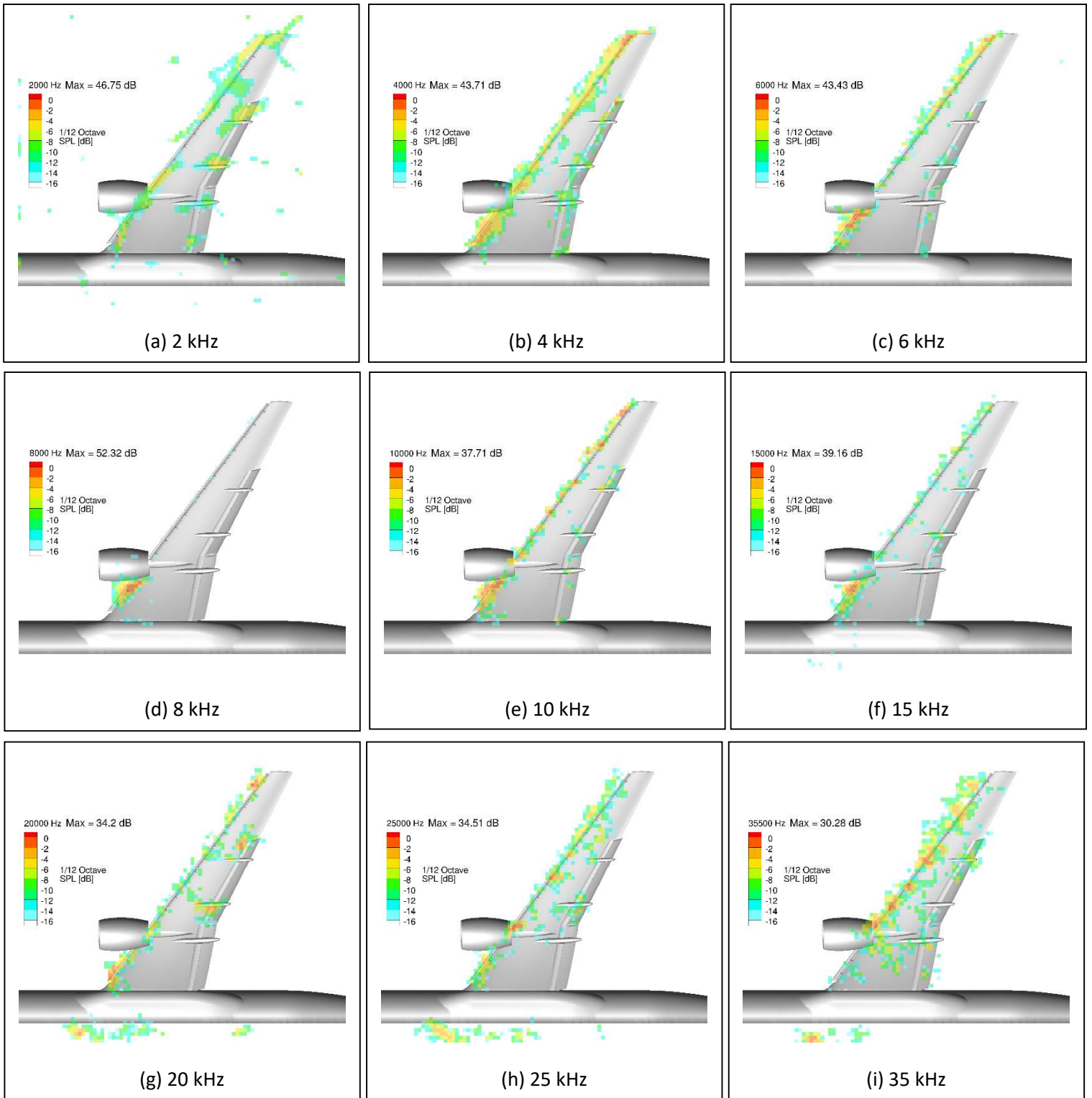


**Figure 14. 1/12-octave band MCF-DAMAS output.**  
**Baseline PSS (Configuration 2),  $\alpha = 8.5^\circ$ ,  $M = 0.16$ ,  $\phi = 90^\circ$ .**

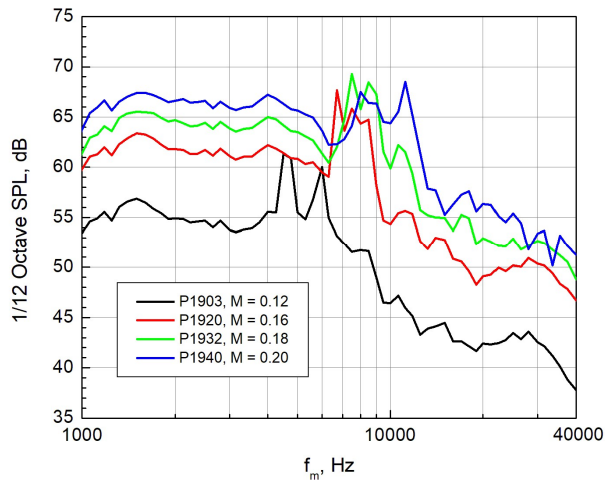


**Figure 15. Baseline PSS (Configuration 2)  
Mach Number Effects,  $\alpha = 8.5^\circ$ ,  $\phi = 90^\circ$ .**

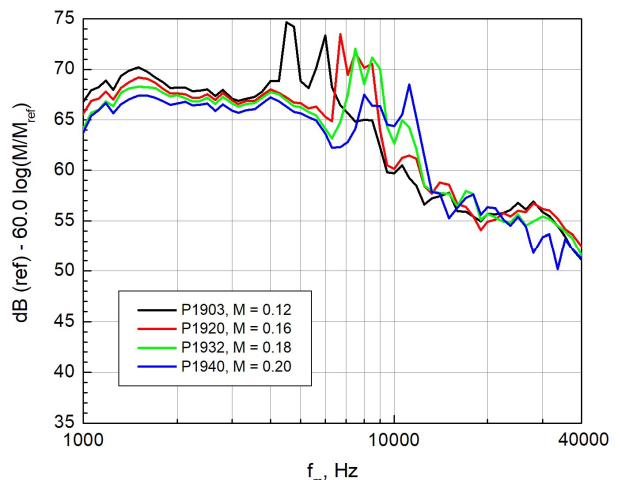


**Figure 16. Baseline PSS (Configuration 2)  
Mach Number Scaling,  $\alpha = 8.5^\circ$ ,  $\phi = 90^\circ$ .**

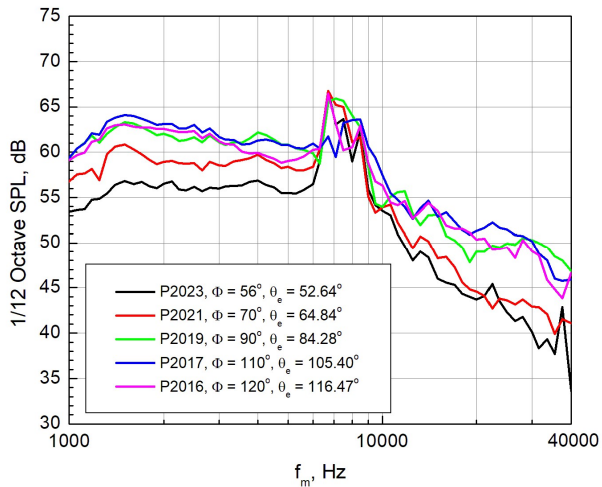


**Figure 17. Baseline PSS (Configuration 2)  
Directivity,  $\alpha = 8.5^\circ$ ,  $M = 0.16$ ,  $\phi = 90^\circ$ .**

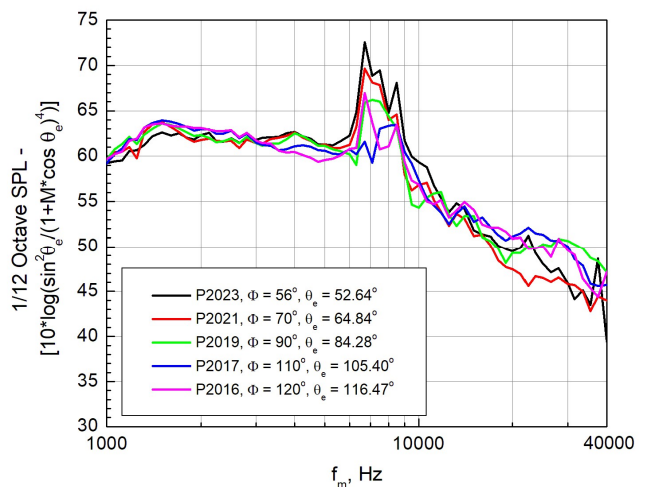


**Figure 18. Baseline PSS (Configuration 2)  
Scaled Directivity,  $\alpha = 8.5^\circ$ ,  $M = 0.16$ ,  $\phi = 90^\circ$ .**

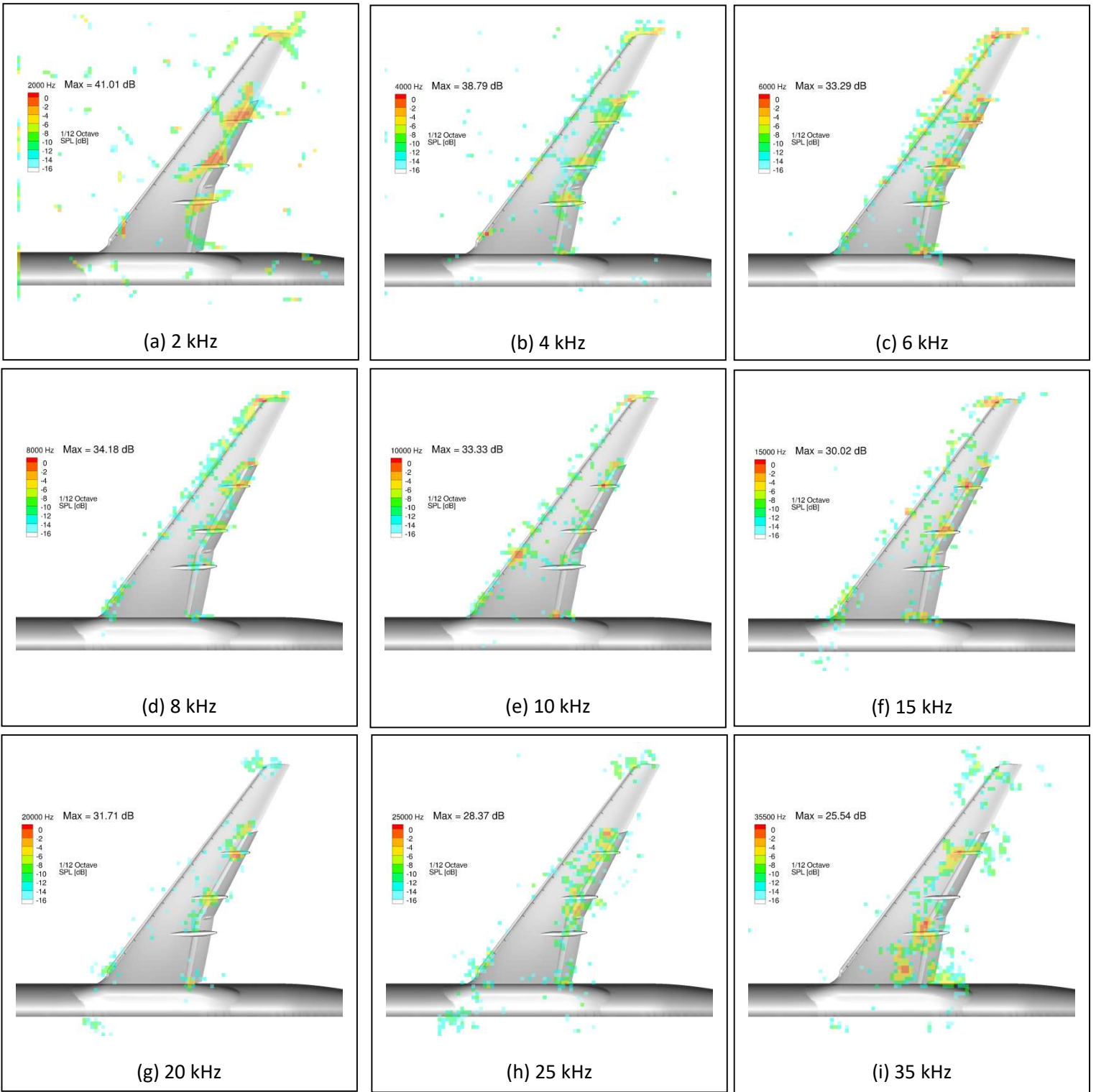


**Figure 19. 1/12-octave band MCF-DAMAS output.**  
**FSS with SGF (Configuration 3),  $\alpha = 8.5^\circ$ ,  $M = 0.16$ ,  $\phi = 90^\circ$ .**

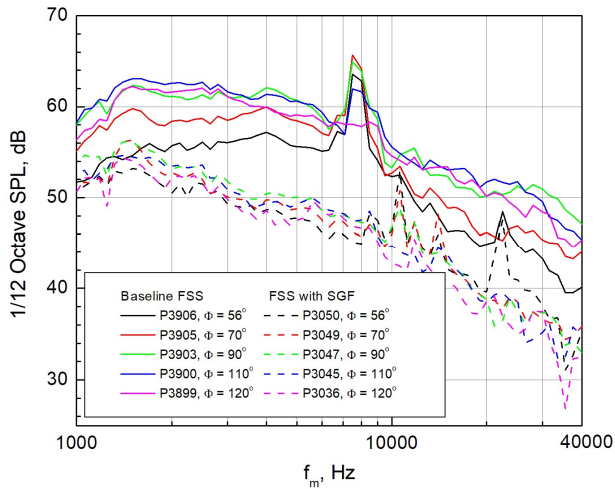


**Figure 20. Comparison of Configurations 1 and 3 (Baseline FSS and FSS with SGF),  $\alpha = 8.5^\circ$ ,  $M = 0.16$ .**

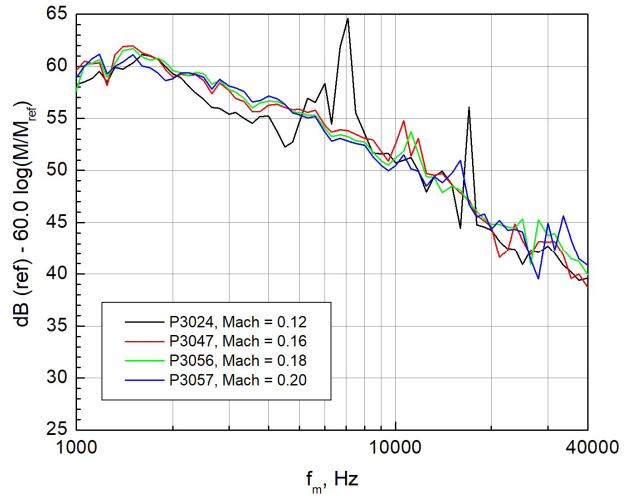


**Figure 21. FSS / SGF (Configuration 3) Mach Number Scaling,  $\alpha = 8.5^\circ$ ,  $\phi = 90^\circ$ .**

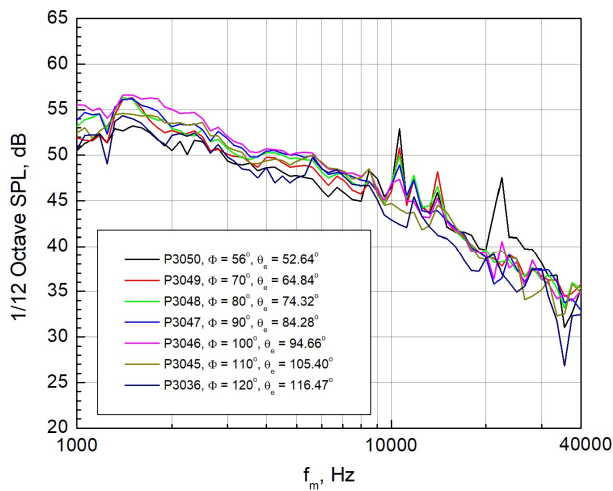


**Figure 22. FSS / SGF (Configuration 3) Directivity,  $\alpha = 8.5^\circ$ ,  $M = 0.16$ .**

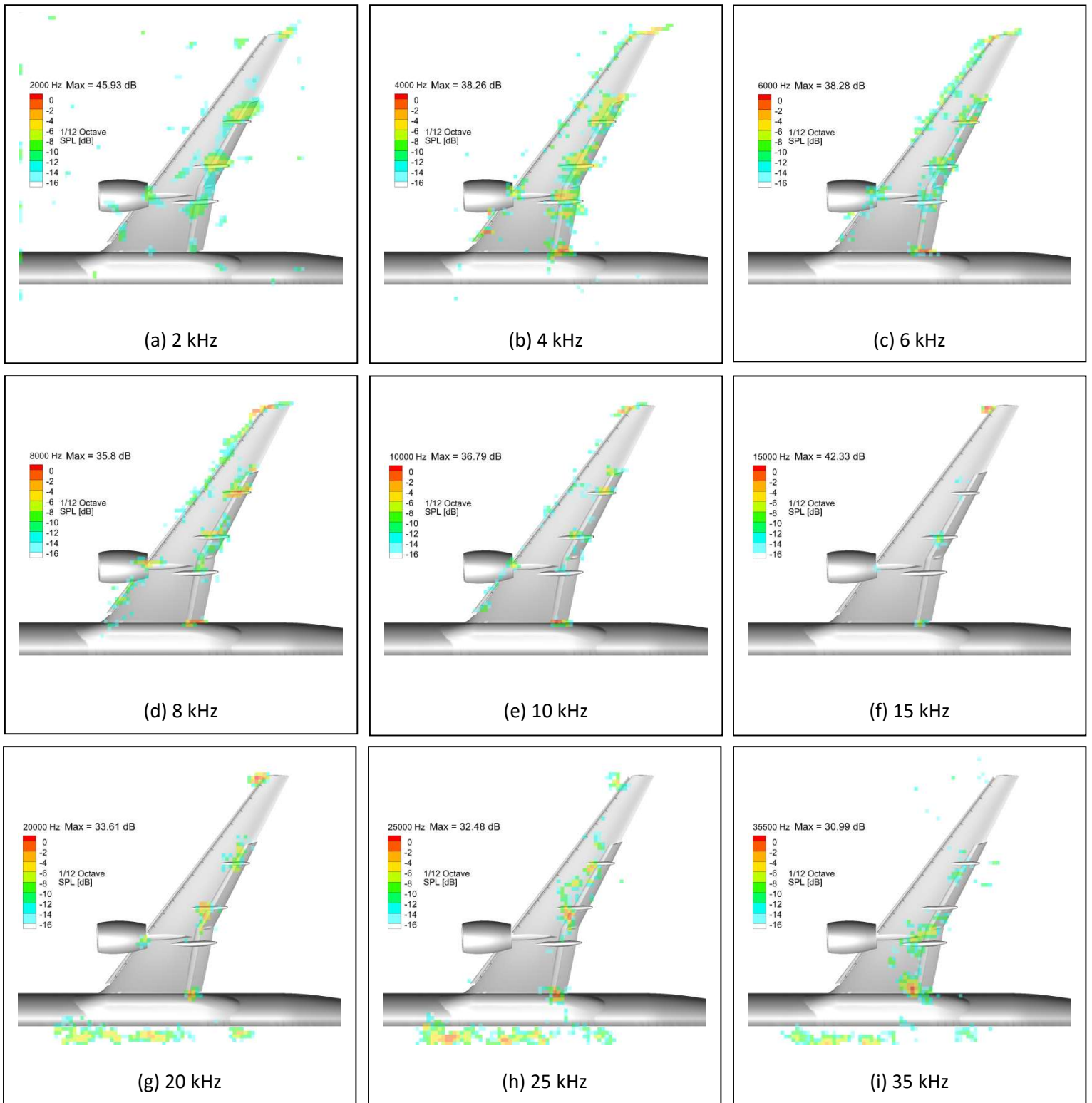


**Figure 23. 1/12th-octave band MCF-DAMAS output.  
PSS with SGF (Configuration 4),  $\alpha = 8.5^\circ$ ,  $M = 0.16$ ,  $\phi = 90^\circ$ .**

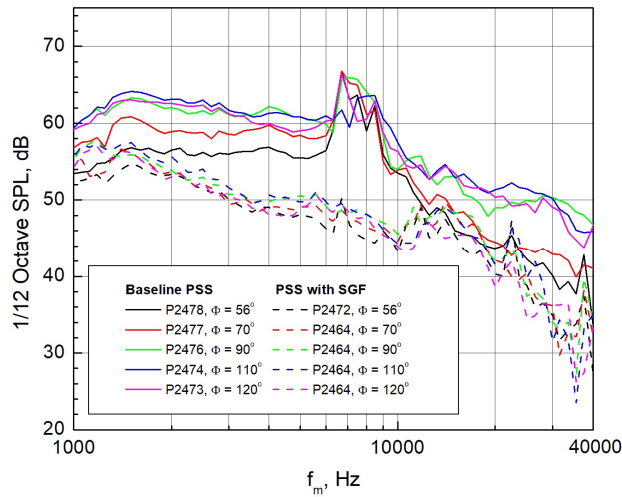


**Figure 24. Comparison of Configurations 2 and 4 (Baseline PSS and PSS with SGF),  $\alpha = 8.5^\circ$ ,  $M = 0.16$ .**

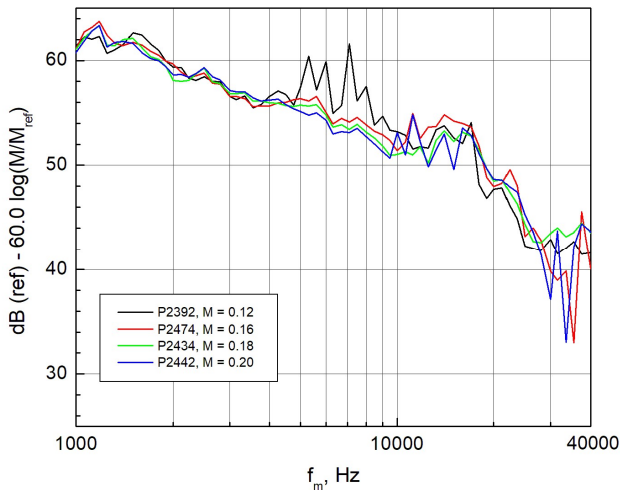


**Figure 25. PSS with SGF (Configuration 4) Mach Number Scaling,  $\alpha = 8.5^\circ$ ,  $\phi = 90^\circ$ .**

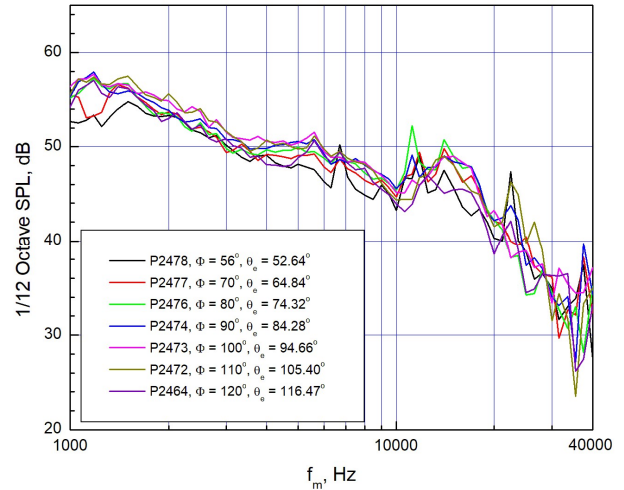


**Figure 26. PSS with SGF (Configuration 4) Directivity,  $\alpha = 8.5^\circ$ ,  $M = 0.16$ .**



**Figure 27. High-fidelity Main Landing Gear:**  
**(a) Position on Model, (b) Closeup View**

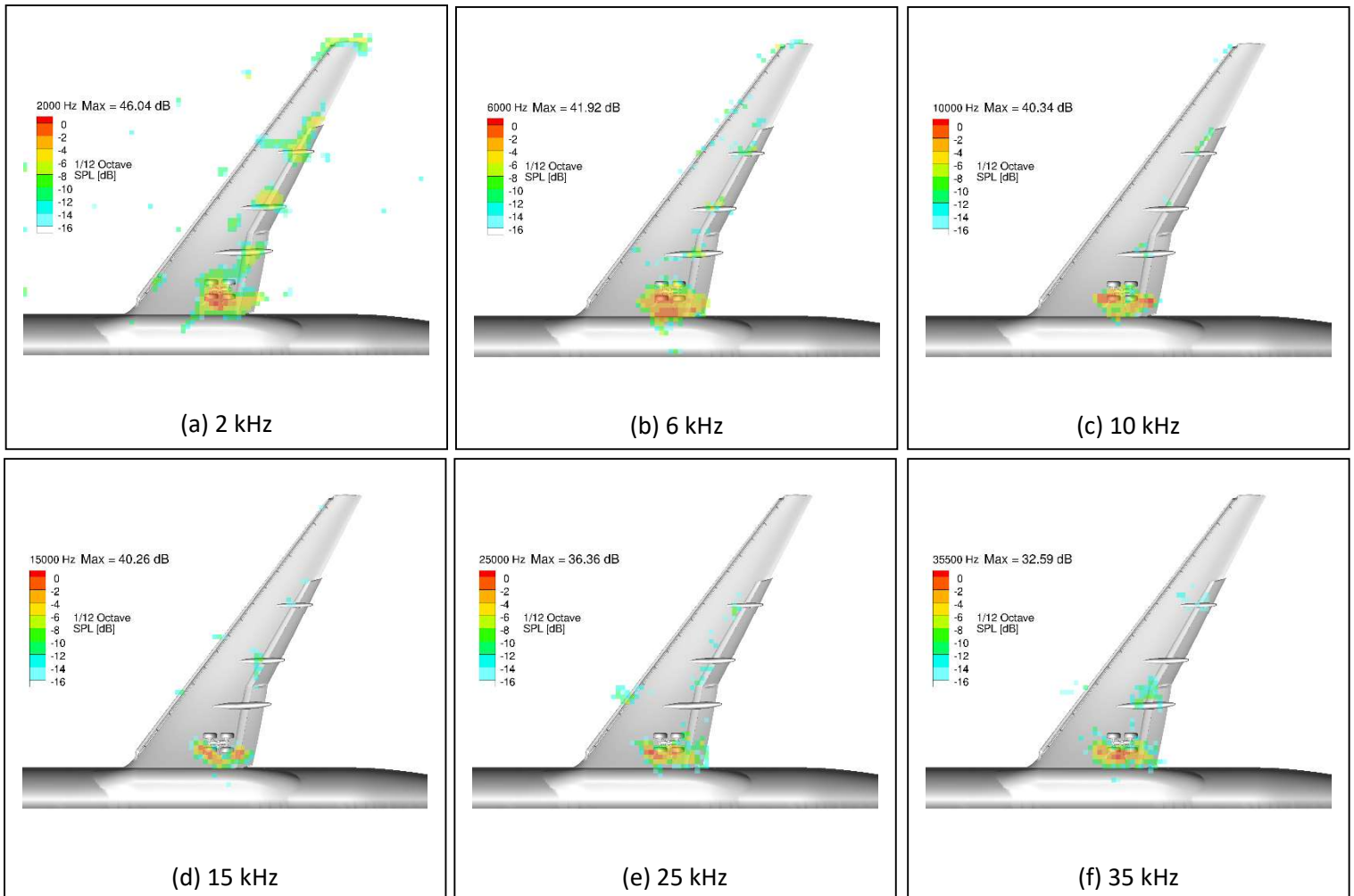


**Figure 28. 1/12th-octave band MCF-DAMAS output.**  
**FSS with SGF and MLG (Configuration 5),  $\alpha = 8.5^\circ$ ,  $M = 0.16$ ,  $\phi = 90^\circ$ .**

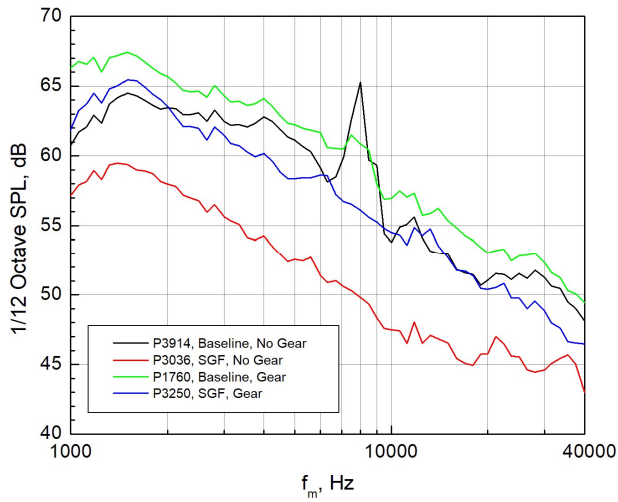


**Figure 29. FSS / MLG Noise Comparison (Configuration 5),  $\alpha = 8.5^\circ$ ,  $M = 0.16$ ,  $\phi = 90^\circ$ .**

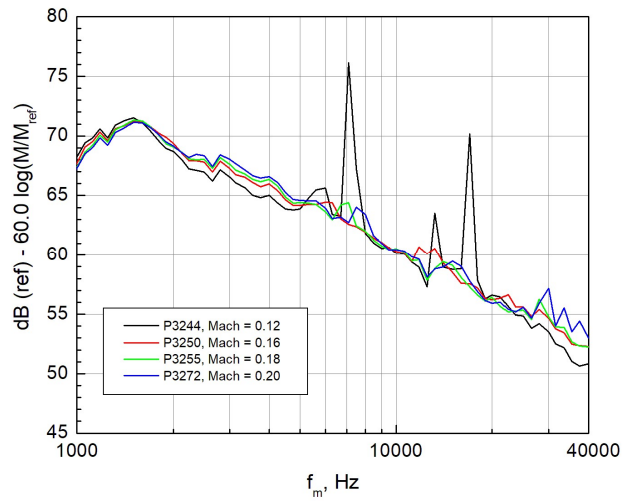


**Figure 30. FSS / MLG Mach Number Scaling (Configuration 5),  $\alpha = 8.5^\circ$ ,  $\phi = 90^\circ$ .**

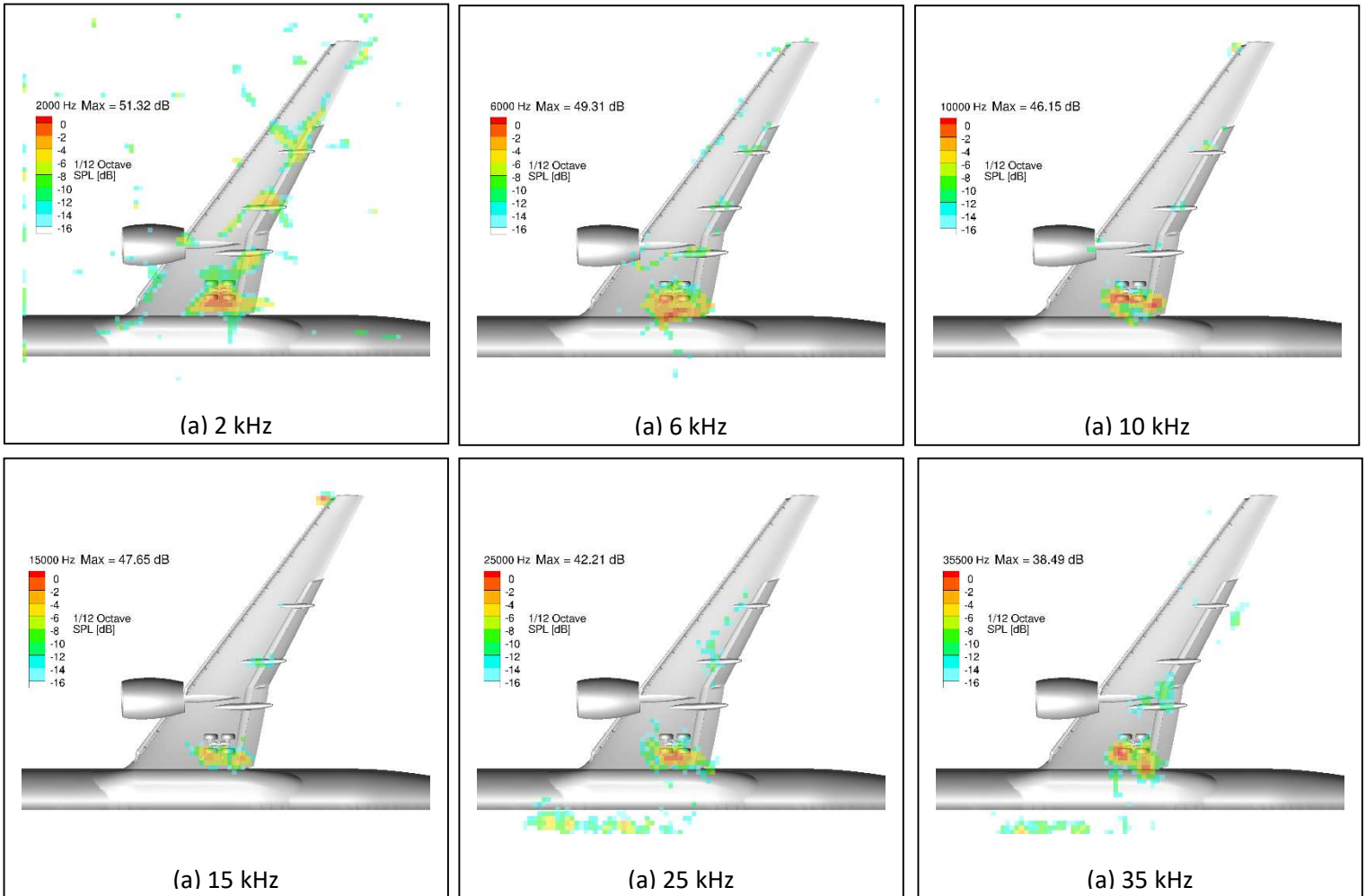


**Figure 31. 1/12th-octave band MCF-DAMAS output. PSS with SGF and MLG (Configuration 6),  $\alpha = 8.5^\circ$ ,  $M = 0.16$ ,  $\phi = 90^\circ$ .**

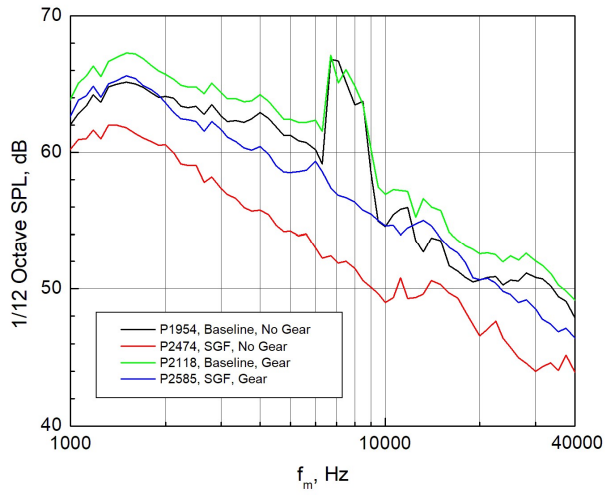


**Figure 32. PSS / MLG Noise Comparison (Configuration 6),  $\alpha = 8.5^\circ$ ,  $M = 0.16$ ,  $\phi = 90^\circ$ .**

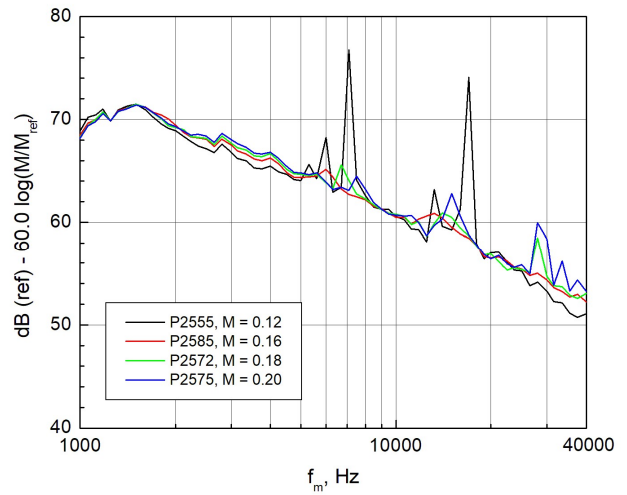


**Figure 33. PSS / MLG Mach Number Scaling (Configuration 6),  $\alpha = 8.5^\circ$ ,  $\phi = 90^\circ$ .**

**Appendix I. Phased Array Stations and Equivalent Emission Angles.**

<b>Mach #</b>	<b>Array Station, <math>\phi</math>, degrees</b>	<b>Array Tunnel Streamwise Location, meters (inches)</b>	<b>Observer Emission Angle, <math>\theta_e</math>, degrees</b>
0.00	56.00	2.15 (84.98)	55.35
0.00	60.00	2.64 (103.98)	59.25
0.00	70.00	3.74 (147.42)	69.44
0.00	80.00	4.71 (185.61)	79.70
0.00	90.00	5.63 (221.50)	90.00
0.00	100.00	6.54 (257.39)	100.30
0.00	110.00	7.51 (295.58)	110.56
0.00	120.00	8.61 (339.02)	120.75
0.12	56.00	2.15 (84.98)	53.18
0.12	60.00	2.64 (103.98)	56.62
0.12	70.00	3.74 (147.42)	65.92
0.12	80.00	4.71 (185.61)	75.63
0.12	90.00	5.63 (221.50)	85.70
0.12	100.00	6.54 (257.39)	96.08
0.12	110.00	7.51 (295.58)	106.73
0.12	120.00	8.61 (339.02)	117.60
0.16	56.00	2.15 (84.98)	52.64
0.16	60.00	2.64 (103.98)	55.91
0.16	70.00	3.74 (147.42)	64.84
0.16	80.00	4.71 (185.61)	74.32
0.16	90.00	5.63 (221.50)	84.28
0.16	100.00	6.54 (257.39)	94.66
0.16	110.00	7.51 (295.58)	105.40
0.16	120.00	8.61 (339.02)	116.47
0.18	56.00	2.15 (84.98)	52.42
0.18	60.00	2.64 (103.98)	55.58
0.18	70.00	3.74 (147.42)	64.32
0.18	80.00	4.71 (185.61)	73.68
0.18	90.00	5.63 (221.50)	83.57
0.18	100.00	6.54 (257.39)	93.94
0.18	110.00	7.51 (295.58)	104.73
0.18	120.00	8.61 (339.02)	115.89
0.20	56.00	2.15 (84.98)	52.22
0.20	60.00	2.64 (103.98)	55.28
0.20	70.00	3.74 (147.42)	63.81
0.20	80.00	4.71 (185.61)	73.04
0.20	90.00	5.63 (221.50)	82.87
0.20	100.00	6.54 (257.39)	93.23
0.20	110.00	7.51 (295.58)	104.06
0.20	120.00	8.61 (339.02)	115.31